

InverseCrafter: Efficient Video ReCapture as a Latent Domain Inverse Problem

Yeobin Hong^{1*} Suhyeon Lee^{1*} Hyungjin Chung^{2†} Jong Chul Ye^{1†}
¹KAIST ²EverEx

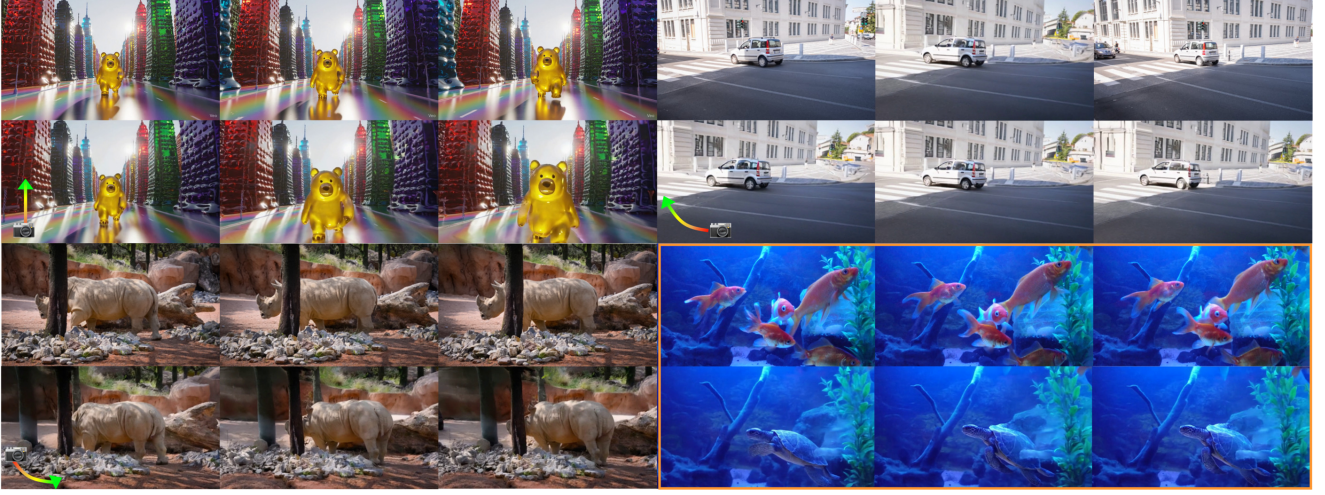


Figure 1. **Representative video** on camera control ("zoom in," "arc left," "arc right") and inpainting with editing ("goldfish" to "turtle").

Abstract

Recent approaches to controllable 4D video generation often rely on fine-tuning pre-trained Video Diffusion Models (VDMs). This dominant paradigm is computationally expensive, requiring large-scale datasets and architectural modifications, and frequently suffers from catastrophic forgetting of the model’s original generative priors. Here, we propose **InverseCrafter**, an efficient inpainting inverse solver that reformulates the 4D generation task as an inpainting problem solved in the latent space. The core of our method is a principled mechanism to encode the pixel space degradation operator into a continuous, multi-channel latent mask, thereby bypassing the costly bottleneck of repeated VAE operations and backpropagation. InverseCrafter not only achieves comparable novel view generation and superior measurement consistency in camera control tasks with near-zero computational overhead, but also excels at general-purpose video inpainting with editing. Code is available at <https://github.com/yeobinhong/InverseCrafter>.

1. Introduction

The ability to generate and interact with dynamic, 4D scenes is a foundational goal in computer vision, with transforma-

tive potential for industries ranging from AR/VR and gaming to filmmaking and digital twins. Video Diffusion Models (VDMs) [6, 8, 18, 26, 51] have emerged as a state-of-the-art solution for generating diverse and photorealistic video content. However, their control mechanism is typically limited to coarse inputs, such as text descriptions or a first frame conditioning image. This fundamental limitation prevents their direct application to 4D synthesis, which demands precise control over camera trajectories and temporal evolution.

One promising branch of research that has emerged to address the challenge for 4D synthesis is the framing of the problem as a video-to-video translation task: given a user input video, synthesize novel views over time while following a target camera trajectory (e.g., camera control). A line of work fine-tunes VDMs to condition on prospective cameras [3, 50, 55], which requires large-scale 4D datasets and still generalizes poorly to unseen camera trajectories. Another branch [15, 42, 56, 61] reframes the task as 3D-aware inpainting (see Fig. 2(a-1)). These methods leverage 3D reconstruction priors (e.g., depth estimation or point tracking) to first generate large-scale, pseudo-annotated datasets and then fine-tune the VDM to inpaint the occluded regions. This training process often creates a strong dependency on the specific 3D reconstruction model used during training. Furthermore, some methods additionally modify the VDM

* Equal contribution, † Co-corresponding author

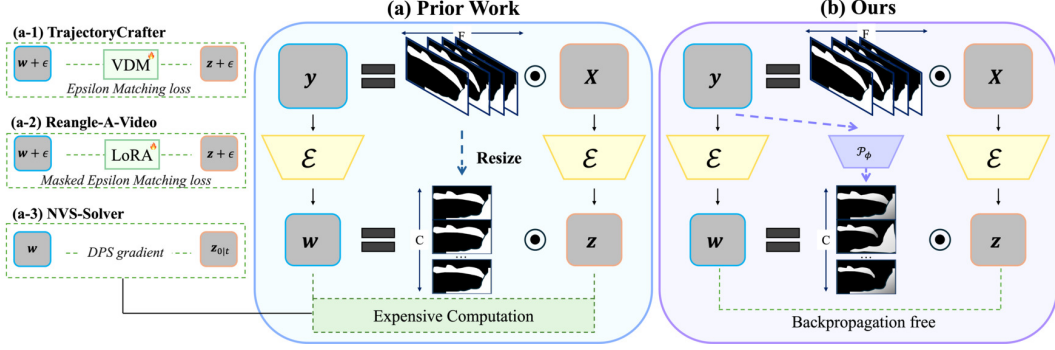


Figure 2. (a) Prior work naively downsamples the pixel space mask via spatio-temporal interpolation. This process results in a single-channel, binary mask that is uniformly broadcast across all C latent channels, ignoring their distinct feature representations and leading to information loss. (b) InverseCrafter computes a continuous, C -channel latent mask, enabling efficient latent-space guidance.

architecture to augment the VDM architecture (*e.g.*, adding new attention blocks [56, 61]), substantially increasing inference latency. Fine-tuning also induces overfitting and catastrophic forgetting, degrading the pretrained model’s general text-to-video generation capabilities and preventing it from functioning as a versatile generative prior. Alternatively, per-video optimization approaches [21] avoid large-scale re-training as shown in Fig. 2(a-2), but they overfit to individual scenes and fail to generalize.

A promising, training-free alternative formulates 4D video generation as an inverse problem, where the warped video serves as a measurement. However, adapting diffusion inverse solvers from the image domain to video inpainting presents several challenges. For instance, NVS-Solver [60] in Fig. 2 (a-3) utilizes Diffusion Posterior Sampling (DPS) [11]. Applying computationally expensive backpropagation [11] required for DPS through the VDM at every sampling step is impractical. Conversely, backpropagation-free solvers [12, 52] are often restricted to (near) linear inverse problems, making them unsuitable for this non-linear inpainting task¹. Furthermore, a critical flaw plagues nearly all recent video inpainting methods [21, 38, 60, 61] as they naively resize pixel space masks to the latent domain, incorrectly assuming that spatio-temporal features and relationships are preserved in the latent domain.

To address this clear gap, we present InverseCrafter, which introduces a principled mechanism to project pixel space masks (m) into a high-fidelity *continuous* latent mask (h) (see Fig. 2(b)). This core contribution enables the adaptation of a computationally efficient inverse solver that operates entirely within the VDM’s latent space. We present two highly effective options - a learned mask encoder or a training-free projection. Both approaches produce a high-fidelity latent mask that respects the VAE’s channel-dependent representations, a critical step that prior work overlooks. By performing guidance entirely in the latent space, our method avoids the costly bottleneck of VAE en-

coding/decoding and backpropagation at every sampling step, drastically reducing computation time. Our main contributions are summarized as follows:

- We introduce a novel *InverseCrafter* that formulates controllable 4D video generation as an inverse problem, enabling the use of pre-trained VDMs without fine-tuning.
- We propose a general and efficient backpropagation-free inpainting inverse solver that operates entirely in the latent space, supported by a continuous mask representation.
- Our framework achieves near-zero additional inference cost over standard diffusion inference while producing high-fidelity, spatio-temporally coherent videos.

2. Preliminaries

Video Inpainting for 4D Generation. Recent works [15, 42, 56, 61] frame 4D video-to-video translation task as an inpainting problem by generating conditional inputs using a 3D reconstruction model and then fine-tuning the VDM to inpaint the occluded regions. Other works have attempted to solve the video re-angling task using training-free methods by adapting diffusion inverse solvers. For instance, NVS-Solver [60] employed diffusion Posterior Sampling (DPS). To mitigate the prohibitive computational cost associated with VAE decoding and gradient computation at each step, NVS-Solver performs its operations directly in the latent space. Unfortunately, [60] struggles with generalization and stability, as it relies on hand-crafted hyperparameters for specific VDM architectures [6]. On the other hand, Zero4D [38] formulates the 4D video generation as a video interpolation problem in the latent domain by employing mask resizing and a subsequent mask-based interpolation between the generated output and the measurement. A critical limitation of these approaches is their reliance on models like Stable Video Diffusion (SVD) [6], whose VAE performs spatial compression only. Both methods project the degradation operator (pixel space mask) into the latent space via simple average pooling over the spatial dimensions. This challenge

¹The problem is non-linear in the latent space due to the VAE encoder.

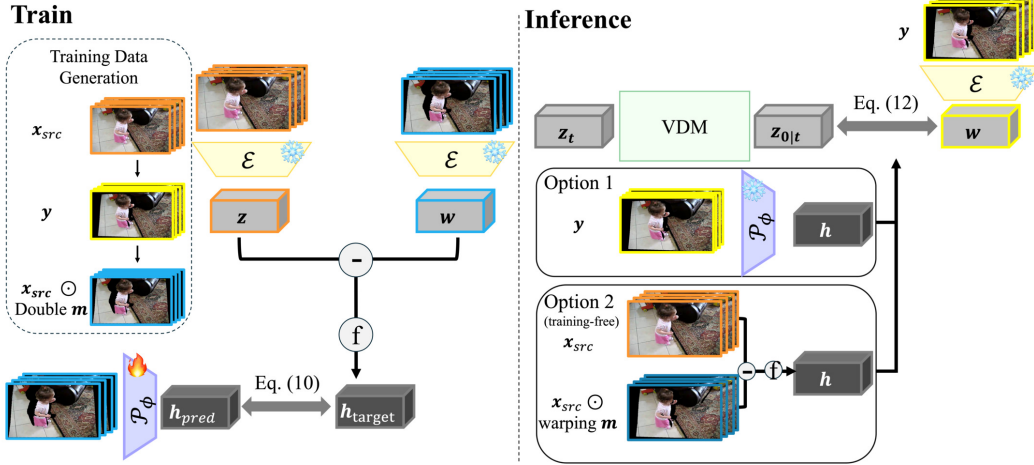


Figure 3. **Overview of InverseCrafter.** (a) \mathcal{P}_ϕ is trained to project the pixel space degradation operator to the latent domain. (b) During inference, z_t is optimized at each t to enforce data consistency Eq. (8), the latent mask derived from either \mathcal{P}_ϕ or the training-free alternative.

of correctly formulating the measurement and masking operation in the latent space is a common, unaddressed issue. Heuristics to spatially compressing the mask are inherited from the image diffusion literature, where inverse solvers either decode to pixel space or apply an arbitrarily resized masking operator in the latent space. The problem of binary resizing is significantly exacerbated when it comes to modern Video Diffusion Models (VDMs). Since modern VDMs utilize 3D VAEs for spatio-temporal compression, mapping a 2D pixel space mask to a 3D latent space is ill-defined.

Diffusion Models for Inverse Problems. Consider the following forward problem:

$$\mathbf{y} = \mathcal{A}(\mathbf{x}) + \mathbf{n}, \quad (1)$$

where \mathcal{A} is the forward mapping and \mathbf{n} is additive noise. Then, the goal of the inverse problem is to retrieve \mathbf{x} from the corrupted \mathbf{y} . While diffusion models are trained to sample from $p(\mathbf{x})$, diffusion model-based inverse problem solvers can guide the generation process during inference time to perform approximate posterior sampling $\mathbf{x} \sim p(\mathbf{x}|\mathbf{y})$ [14]. Notably, *all* zero-shot methods aim to minimize the data consistency $\|\mathbf{y} - \mathcal{A}(\mathbf{x})\|^2$ during the sampling process. For pixel-based diffusion models, this is relatively straightforward, as the estimates during generation remain in the pixel space. In contrast, using these solvers with LDMs—which dominate modern literature—requires special treatment. Most solvers that operate in the latent space [13, 24, 44, 47] first decode the estimated latent to the pixel space, and measure the consistency in the decoded pixel space. The process of correcting the latent further induces approximation errors and heavy computation, often leading to blurry samples. Recently, SILO [41] proposed to mitigate this gap by training a network to estimate the *latent* forward model, so that one can bypass the need for decoding to pixel space during sampling,

leading to competitive results in standard image restoration tasks. Motivated by SILO, in this work, we devise ways to solve the dynamic NVS task purely in the latent space.

3. InverseCrafter

Problem Formulation. To solve the inverse problem of novel view synthesis, we must formulate the measurement \mathbf{y} based on 3D geometric constraints. This requires projecting the source video into a target camera view. First, we establish a 3D representation of the scene. We process the source video $\mathbf{x}_{1:F}$ frame-by-frame using a pre-trained monocular depth estimation network [19] to acquire a per-frame estimated depth map $\hat{\mathbf{D}}_{1:F}$. Next, for each frame i , we unproject the 2D pixel coordinates (from the image \mathbf{x}_i) into a 3D point cloud \mathbf{P}_i using the estimated depth $\hat{\mathbf{D}}_i$ and an intrinsic camera matrix \mathbf{K} . This back-projection function is denoted Π^{-1} :

$$\mathbf{P}_i = \Pi^{-1}(\mathbf{x}_i, \hat{\mathbf{D}}_i, \mathbf{K}). \quad (2)$$

Once the scene is represented in 3D, we can render it from a new perspective. The 3D point cloud \mathbf{P}_i is transformed into the target camera’s coordinate system using a relative transformation matrix \mathbf{T}_i . These transformed points are then projected back into a 2D image \mathbf{y}_i using the forward projection function Π :

$$\mathbf{y}_i = \Pi(\mathbf{T}_i \cdot \mathbf{P}_i, \mathbf{K}). \quad (3)$$

The warped video $\mathbf{y} := \mathbf{y}_{1:F}$ represents the pixel space measurement, which contains occlusions from the 3D warping process, which can be succinctly written as

$$\mathbf{y} = \mathbf{m} \odot \mathbf{x}, \quad \mathbf{x}, \mathbf{y}, \mathbf{m} \in \mathbb{R}^N \quad (4)$$

where \odot denotes the element-wise product and $N = FHW$ is the pixel space resolution, and \mathbf{m} refers to a binary mask indicating the occlusion from the 3D warping process.

Recent video diffusion models [51, 59] introduce 3D VAEs that perform spatiotemporal compression, creating the need to reformulate the pixel-domain forward model in Eq. (4) in the latent domain. These architectures map pixel resolutions (F, H, W) to latent resolutions (f, h, w) , where spatial dimensions are reduced by a factor of 8, similar to image VAEs, and the temporal dimension is commonly compressed by a factor of 4. Inference-time image inpainting methods for latent diffusion models [22, 23] typically construct latent masks by projecting pixel-space masks into the latent space via an $8\times$ downsampling with nearest-neighbor interpolation. However, the additional temporal compression in video models necessitates special consideration beyond these image-based techniques.

Nevertheless, recent video inpainting methods that operate directly in the latent domain [21, 56, 61] largely adopt direct spatiotemporal projection (*i.e.*, spatiotemporal interpolation) as a naive extension of image-based approaches. This practice relies on several problematic assumptions. First, it implicitly assumes that spatial structures in pixel space are preserved under the non-linear VAE encoder, which is generally false. Second, it treats the latent mask as uniform across channels, despite the fact that latent channels encode highly heterogeneous feature representations, as illustrated in Fig. 2(a) (visualizations in Appendix C.1). Third, some methods [21, 61] adopt an overly conservative temporal rule: a latent region is marked as “known” only if its corresponding pixel region is visible in all frames within its temporal group. This strategy becomes a major bottleneck for videos with fast motion. If an object appears in only a subset of frames due to rapid movement or partial occlusion, the entire corresponding latent region is marked as “unknown,” which forces unnecessary inpainting and increases reliance on the generative model, as shown in Fig. 8(a).

Generating Continuous Mask. To address the mask projection inconsistencies outlined previously, we propose learning a lightweight neural network, dubbed the mask encoder $\mathcal{P}_\phi(\cdot) : \mathbb{R}^N \rightarrow \mathbb{R}^{C \times M}$, where C denotes the number of latent channels and $M = fhw$ represents the latent-space resolution, to compute an accurate latent-space mask that takes in as input the pixel measurement \mathbf{y} and outputs a continuous mask that can be applied *linearly* to the latent \mathbf{z} , with the same Hadamard product operation as in Eq. (4).

Our training target is derived from the observation that autoencoders are effective at reconstructing degraded data [41]. We define this ground-truth latent mask, $\mathbf{h} \in \mathbb{R}^{C \times M}$, as the normalized difference between the latent encoding of the clean video, $\mathcal{E}(\mathbf{x})$, and the latent encoding of the masked video, $\mathcal{E}(\mathbf{m} \odot \mathbf{x})$:

$$\mathbf{h} = \mathbf{f}(\mathcal{E}(\mathbf{x}) - \mathcal{E}(\mathbf{m} \odot \mathbf{x})), \quad (5)$$

where \mathbf{f} stands for normalization using an activation function,

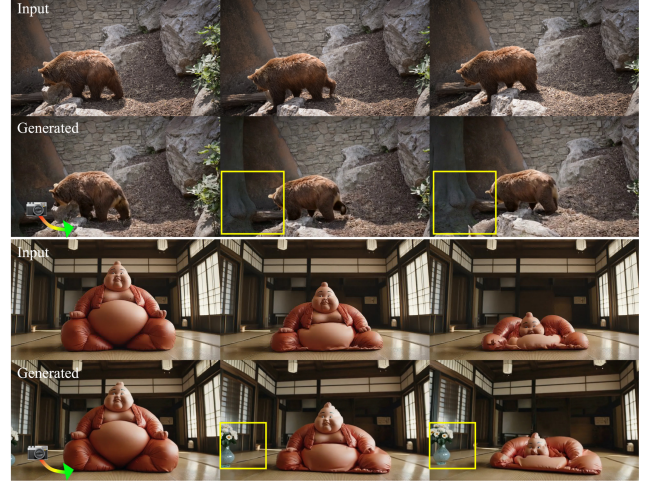


Figure 4. **Video camera control results with novel content generation.** (Up) “+a grey tree.” (Bottom) “+a flower vase.”

scaling the latent difference to a $[0, 1]$ range.

However, a primary challenge is obtaining training pairs, as for generating warped videos (Eq. (3)), the corresponding “ground truth” video \mathbf{x} is not available. To resolve this, we employ a double-reprojection strategy from [61] to synthesize the correctly masked counterpart $\mathbf{m} \odot \mathbf{x}$ from the clean video \mathbf{x} , which provides the necessary pair to compute \mathbf{h} .

The mask encoder is then trained to predict this ground-truth latent mask directly from the pixel space mask with a combination of the L1 loss and the Structural Similarity Index Measure (SSIM) [53] loss:

$$\min_{\phi} (\|\mathcal{P}_\phi(\mathbf{y}) - \mathbf{h}\|_1 + \lambda(1 - \text{SSIM}(\mathcal{P}_\phi(\mathbf{y}), \mathbf{h}))) \quad (6)$$

Unlike naive mask resizing, which generates a single-channel binary mask that is uniformly broadcast across all C latent channels (ignoring their distinct feature representations), our mask encoder outputs a continuous, C -channel mask. This high-fidelity representation better captures the mask’s influence across the latent features, leading to improved VAE reconstruction and superior measurement consistency in final generated outputs, as detailed in Fig. 7-(a).

Furthermore, for tasks such as video inpainting with editing (detailed in Section 4.3.2), where a valid ground-truth latent mask \mathbf{h} is available at inference time, \mathcal{P}_ϕ can be bypassed. In addition, we empirically found that a training-free strategy is also possible for the video camera control task. Specifically, we compute an approximate latent mask on-the-fly as $\mathbf{h} = \mathbf{f}(\mathcal{E}(\mathbf{x}_{src}) - \mathcal{E}(\mathbf{m}_{warp} \odot \mathbf{x}_{src}))$. While the trained \mathcal{P}_ϕ is optimized to achieve superior VAE reconstruction and measurement consistency (as shown in Table 1 and Fig. 7(a)), we emphasize that this training-free alternative attains reasonable generative quality without any training cost. A key advantage of our framework is its flexibility, supporting both the learned and the training-free variants of

Algorithm 1 Algorithm of InverseCrafter

Require: Source video x_{src} , pixel space measurement y , pixel space mask m , image-to-video flow-based model v^θ , VAE encoder and Decoder \mathcal{E}/\mathcal{D} , measurement consistency hyperparameter Γ , CG iteration K

```
1: if use  $\mathcal{P}_\phi$  then
2:    $h \leftarrow \mathcal{P}_\phi(y)$ 
3: else
4:    $h \leftarrow f(\mathcal{E}(x_{src}) - \mathcal{E}(m \odot x_{src}))$ 
5: end if
6: Initialization  $z_T \sim \mathcal{N}(0, \mathbf{I})$ 
7:  $w \leftarrow \mathcal{E}(y)$ 
8:  $\mathbf{H} \leftarrow \text{diag}(h)$ 
9: for  $t : 1 \rightarrow 0$  do
10:   $\triangleright$  Tweedie denoising
11:   $\hat{z}_{0|t} = z_t - v^\theta(z_t)t$ 
12:   $\hat{z}_{1|t} = z_t + v^\theta(z_t)(1 - t)$ 
13:  if  $t \in \Gamma$  then
14:     $\triangleright$  Data consistency
15:     $\hat{z}(y) \leftarrow \text{CG}(\mathbf{I} + \gamma \mathbf{H}^\top \mathbf{H}, \hat{z}_{0|t} + \gamma \mathbf{H}^\top w, \hat{z}_{0|t}, K)$ 
16:     $z_{t-1} \leftarrow \text{ODESolve}(\hat{z}(y), \hat{z}_{1|t})$ 
17:  else
18:     $z_{t-1} \leftarrow \text{ODESolve}(\hat{z}_{0|t}, \hat{z}_{1|t})$ 
19:  end if
20: end for
21:  $x_{tgt} \leftarrow \mathcal{D}(z_0)$ 
```

latent mask generation. Alg. 1 summarizes the full pipeline.

DDS for Latent Inpainting with Continuous Masks. To align with the latent diffusion model, we encode the pixel space measurement into the latent space using the VAE encoder \mathcal{E} . Then, under our noiseless linear setting of Eq. (4), the inverse problem in the pixel domain transforms to an inverse problem in the latent space, i.e.

$$\underbrace{w}_{\mathcal{E}(y)} = \underbrace{h}_{\mathcal{P}_\phi(y)} \odot \underbrace{z}_{\mathcal{E}(x)}, \quad z, w, h \in \mathbb{R}^M. \quad (7)$$

Notice that the design of our mask encoder \mathcal{P}_ϕ is different from that of [41]. The operator encoder used in [41] acts *non-linearly* on the encoded latent z to produce the latent measurement w , whereas our mask encoder produces a continuous linear mask h , which can be applied linearly with a Hadamard product. Thanks to such a design choice, we are free from selecting *any* diffusion model-based inverse problem solvers, even the ones that are specialized for solving linear inverse problems in the pixel space. Among them, we propose to leverage DDS [12]. Namely, the data consistency step of DDS solves the following proximal optimization problem :

$$\min_z \frac{\gamma}{2} \|w - h \odot z\|_2^2 + \frac{1}{2} \|z - \hat{z}_{0|t}\|_2^2, \quad (8)$$

which is followed by the ODE solver. Here, $\hat{z}_{0|t} := \mathbb{E}[z_0|z_t]$ is the estimated posterior mean with the flow model v^θ , and γ is a hyper-parameter that controls the proximal regularization. Following [12], we solve Eq. (8) using conjugate gradient (CG) iterations. Specifically, let $\mathbf{H} := \text{diag}(h)$. Then, Eq. (8) can be solved with $\text{CG}(\mathbf{I} + \gamma \mathbf{H}^\top \mathbf{H}, \hat{z}_{0|t} + \gamma \mathbf{H}^\top w, \hat{z}_{0|t}, K)$ with K iterations.

4. Experimental Results

4.1. Evaluation Details

Task. We evaluate our method on two major video inpainting tasks: video camera control and text-guided video inpainting. Our primary focus is the video camera control task, for which we use 1,000 videos and corresponding captions from the UltraVideo dataset [58]. We sample one of the six target camera trajectories for each video, where the target trajectories are selected following the work in [21]. For text-guided video inpainting, we apply our proposed video inpainting method to replace objects in the video, guided by target text prompts and source object masks. This evaluation is conducted on 20 videos from the DAVIS [39] dataset, along with all available foreground masks. For each video, we generate five target editing prompts using GPT-5-mini [36], while the corresponding source captions used for prompt construction are obtained using BLIP-2 [31].

Evaluation. For the video camera control tasks, we assess performance using a comprehensive set of metrics: measurement consistency metrics - measurement PSNR, LPIPS, SSIM, source consistency metrics - DINO distance [10], Fréchet Video Distance (FVD), and general video quality metrics - subject consistency, temporal flickering, motion smoothness, and overall consistency from VBench [20]. The measurement consistency metric was compared by the warped video, frame by frame. DINO and FVD were calculated by reference to the source video datasets. For video inpainting tasks, we additionally evaluate the generated videos with the editing text-alignment metrics: VLM (see appendix B.2 for details), Clip Score [40] and Pick Score [25].

4.2. Implementation Details

Training. We train our model on the VidSTG [62] dataset. For each of the 7,750 videos in the dataset, we generate 6 double-reprojection datasets from the selected camera trajectories, resulting in a total of 46,500 training samples. We utilize DepthCrafter [19] for monocular depth estimation. Our model architecture is based on the Wan2.1 VAE, which we modify to create a lightweight model by reducing the channel dimension from 96 to 16, resulting in 1.5M parameters. The model is trained at a fixed resolution of 240×416 . We employ the AdamW optimizer [35] with a learning rate of 1×10^{-4} and a weight decay of 3×10^{-2} . Training is conducted with a total batch size of 16, distributed as 4 samples

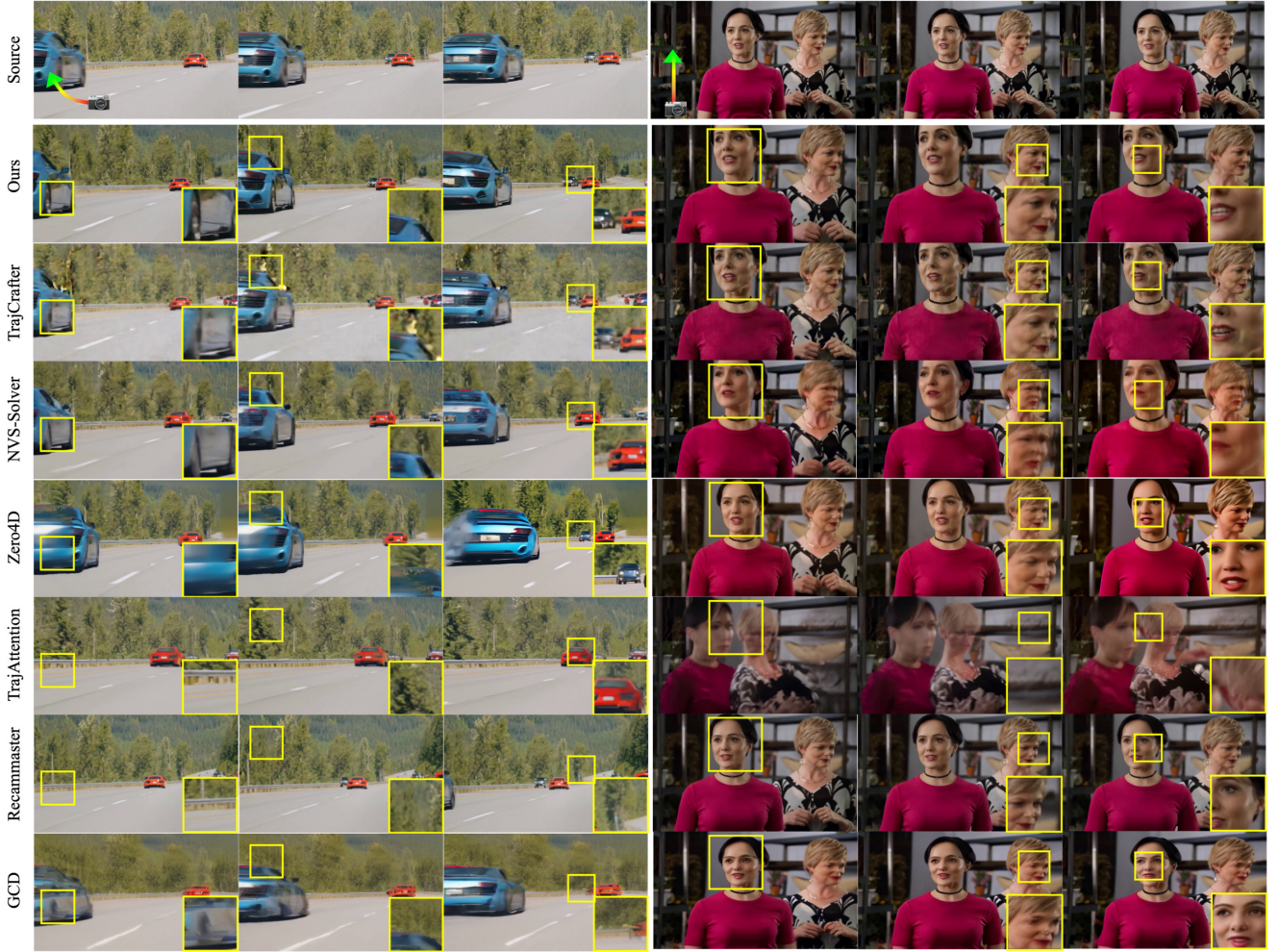


Figure 5. **Qualitative comparison of video camera control.** Camera trajectories are ("arc left" "zoom in"). Our method demonstrates a clear advantage in source consistency and semantically aligned generation. Insets provide magnified views of the regions marked by yellow boxes.

per GPU across 4 GPUs, completed in 1 day.

Inference. In this paper, we use Wan2.1-Fun-V1.1-1.3B-InP [51] at a resolution of 480×832 , a pre-trained image-to-video flow-based model for the main experiments. For encoding masked videos during training or inference, as in [21], we infill the masked region to minimize the train-inference following gap [45]. We use [19] for all training-free methods and TrajectoryCrafter for fair comparison to generate a depth map for each frame.

Compute Resources. All training and inference experiments are conducted using NVIDIA RTX A6000 GPUs (48GB VRAM). A detailed runtime analysis is provided in Table 1.

4.3. Results

4.3.1. Video Camera Control

Table 1 reports results on the video camera control task compared to major baselines. Despite requiring neither additional training data nor VDM fine-tuning, and adding

virtually no overhead beyond standard diffusion inference, our method achieves performance comparable to or better than existing approaches. Furthermore, it delivers consistently strong results across source consistency, measurement consistency, and overall video quality, indicating reliable behavior in practical video generation settings. Notably, methods that depend on large-scale VDM training or heavy gradient-based optimization incur significant computational cost, whereas our approach attains competitive or superior performance while remaining entirely training-free and lightweight.

The qualitative comparisons in Fig. 5 further show that baseline training-based or backpropagation methods (TrajectoryCrafter, NVS-Solver (post), TrajectoryAttention, ReCamMaster) generate artifacts (e.g. in the trees) or fail to faithfully preserve the source video’s content (e.g. background car and women’s faces). Backpropagation-free methods (NVS-Solver (dgs), Zero4D) fail to capture the video’s motion (e.g. background car), generate boundary artifacts,

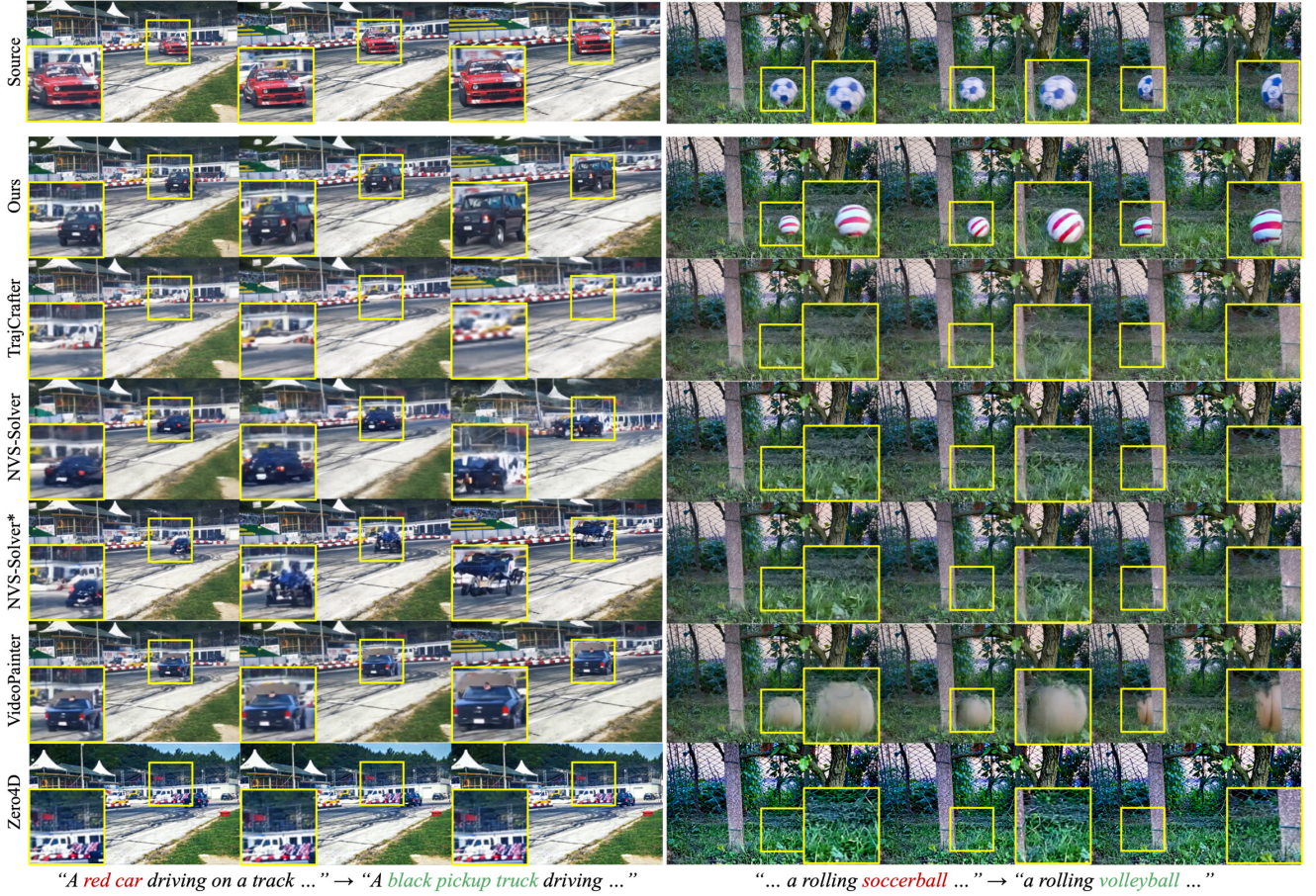


Figure 6. **Qualitative comparison of video inpainting with editing.** InverseCrafter achieves better target text alignment compared to the baselines. NVS-Solver indicates NVS-Solver (post), NVS-Solver* indicates NVS-Solver (dgs).

Table 1. Quantitative evaluation on the camera control task, showing source video consistency and generation quality.

| Method | Runtime | Measurement Consistency | | | Source Consistency | | VBench |
|-----------------------------|-----------|-------------------------|---------------|---------------|--------------------|---------------|---------------|
| | sec ↓ | PSNR ↑ | LPIPS ↓ | SSIM ↑ | DINO ↓ | FVD ↓ | Total Score ↑ |
| TrajAttention [56] | 167 | 19.44 | 0.1405 | 0.6909 | 0.0562 | 233.40 | 0.8756 |
| TrajCrafter [61] | 134 | 28.37 | 0.0573 | 0.8942 | 0.0376 | 120.03 | 0.8954 |
| ReCamMaster [3] | 926 | - | - | - | 0.0504 | 136.28 | 0.8967 |
| GCD [50] | 44 | - | - | - | 0.0691 | 250.85 | 0.8865 |
| NVS-Solver [60] | 696 | 26.68 | 0.0816 | 0.8314 | 0.0393 | 96.90 | 0.8955 |
| Ours | <u>71</u> | 28.95 | 0.0529 | <u>0.8672</u> | <u>0.0369</u> | 102.46 | <u>0.8972</u> |
| Ours (training-free) | <u>71</u> | <u>28.81</u> | <u>0.0534</u> | 0.8652 | 0.0364 | <u>100.21</u> | 0.8976 |

or result in highly saturated videos. On the other hand, our method maintains higher fidelity to the source while preserving visual coherence, demonstrating the practical benefit and reliability of our efficient, training-free formulation.

Furthermore, Fig. 4 highlights our method’s effectiveness in text-conditioned novel content generation. By leveraging the pre-trained VDM as a generative prior, our approach maintains superior semantic alignment, successfully synthesizing contextually consistent content even during complex geometric manipulation.

Table 2. Quantitative evaluation on the text-guided video inpainting task, showing source video consistency and generation quality.

| Method | Source Consistency | | Text Alignment | | | |
|-----------------------------|--------------------|--|-----------------------|---------------|--------------|--------------|
| | FVD ↓ | | Overall Consistency ↑ | VLM ↑ | CLIP Score ↑ | PickScore ↑ |
| TrajCrafter [61] | 1520.08 | | 0.2191 | 0.6140 | 23.88 | 20.24 |
| NVS-Solver [60] | 1648.63 | | 0.2240 | <u>0.6400</u> | 24.94 | 20.52 |
| Zero4D [38] | 2524.49 | | 0.2257 | 0.6260 | 25.83 | 20.79 |
| VideoPainter [5] | <u>1432.77</u> | | <u>0.2287</u> | 0.6290 | <u>25.26</u> | 20.52 |
| Ours (training-free) | 1422.72 | | 0.2289 | 0.6510 | 24.98 | <u>20.56</u> |

4.3.2. Video Inpainting with Editing

As first frame conditioning is essential for I2V models, we provide first-frame conditioning input for training-free methods (NVS-Solver, Zero4D) and VideoPainter, which also utilizes an I2V model. We obtain the first-frame conditioning input using an off-the-shelf image inpainting model [30].

The proposed method outperforms the baselines in source distribution and video text alignment metrics in Table 2. While Zero4D [38] outperforms image based text alignment metrics, this comes from the fact that output video of Zero4D is nearly static as shown in Fig. 6. In the second example, InverseCrafter uniquely generates the volleyball in the masked region, while also matching the measurement, whereas all baselines fail to generate regarding the target text. In both

examples, NVS-Solver (post) deviates a lot from the measurement, NVS-Solver (dgs) and VideoPainter generates boundary artifacts and inferior results. This implies that our method can be used as a general inpainting inverse solver, integrating text descriptions by fully utilizing the pre-trained model’s generative prior.

4.4. Ablation Studies

Fig. 7-(a) compares our continuous latent mask with conventional binary mask resizing using $\times 8$ nearest-neighbor spatially and logical AND downsampling temporally. Our method shows better measurement consistency, where using the trained \mathcal{P}_ϕ shows the best reconstruction, following our training-free version. Fig. 8-(a) shows qualitative comparison of the masking strategies. Reconstructed measurement of binary downsampling doesn’t align with the original measurement due to the conservative masking strategy, failing to properly reconstruct the mask in sequences with fast motion. Conversely, our method generates a consistent continuous mask, thereby preserving the fidelity of the measurement. Fig. 8-(b) compares our method with conventional pixel space DDS as in prior methods [27, 28], which requires additional VAE encoding and decoding at every timestep, a costly bottleneck that our method entirely avoids. Furthermore, as highlighted by the insets, pixel space Conjugate Gradient introduces severe color and textural inconsistencies. In contrast, our proposed method enables seamless integration with measurement without these artifacts.

Fig. 7-(b) and Fig. 8-(c) illustrates the quantitative and qualitative effect of the conjugate gradient hyperparameter Γ on inpainting performance, revealing the trade-off between measurement / source consistency and generation fidelity. We set Γ as $\Gamma = \{t | t \geq 1 - \alpha\}$. When using a larger α (i.e., applying the measurement consistency step earlier in the diffusion process), the result exhibits stronger consistency with the source measurement and improved content faithfulness. In contrast, a smaller α delays the measurement consistency update to later diffusion steps, emphasizing the model’s generative prior and producing more visually refined outputs. This demonstrates that α effectively controls the balance between the diffusion prior and measurement constraints during posterior sampling, where we observe that setting $\alpha = 0.6$ consistently achieves a favorable balance between semantic alignment and structure preservation.

5. Conclusion

In this paper, we presented a novel and efficient framework for novel-view video generation by casting the task as an inverse problem fully defined in the latent space. The core of our method is a principled mechanism for projecting pixel-space masks into continuous, multi-channel latent representations. Our experiments demonstrate that this approach achieves superior measurement consistency while preserv-

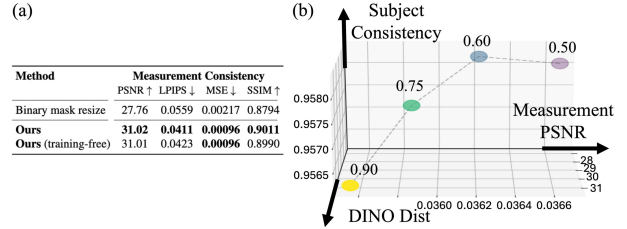


Figure 7. (a) Quantitative results on VAE reconstruction of different masking strategies. (b) Quantitative comparison on Conjugate Gradient Step Hyperparameter α .

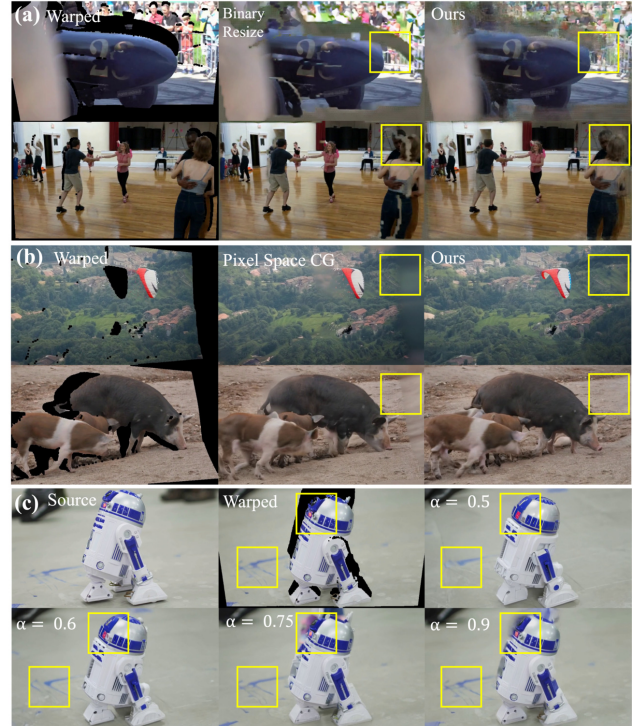


Figure 8. (a) VAE reconstruction of binary downsampled mask and ours. (b) Video camera control results of Pixel Space DDS and ours. (c) Ablation results for α .

ing comparable generation quality in the camera control task. We further show its effectiveness as a general-purpose video inpainting solver for editing tasks. Overall, our framework offers a versatile and lightweight solution for controllable 4D video synthesis, eliminating the need for computationally expensive VDM fine-tuning and incurring no additional inference-time overhead.

Limitations and future work. Although our solver is efficient, its speed is limited by multi-step diffusion sampling process. Our method inherits the pre-trained VDM’s inherent biases. The initial warping stage is a major source of artifacts due to its dependence on potentially inaccurate monocular depth estimates. Finally, while our training-free mask computation is model-agnostic, the learned mask encoder is tailored to a specific VAE architecture.

References

- [1] Sherwin Bahmani, Ivan Skorokhodov, Aliaksandr Siarohin, Willi Menapace, Guocheng Qian, Michael Vasilkovsky, Hsin-Ying Lee, Chaoyang Wang, Jiaxu Zou, Andrea Tagliasacchi, et al. Vd3d: Taming large video diffusion transformers for 3d camera control. *arXiv preprint arXiv:2407.12781*, 2024. 13
- [2] Jianhong Bai, Menghan Xia, Xintao Wang, Ziyang Yuan, Xiao Fu, Zuozhu Liu, Haoji Hu, Pengfei Wan, and Di Zhang. Syncammaster: Synchronizing multi-camera video generation from diverse viewpoints. *arXiv preprint arXiv:2412.07760*, 2024. 13
- [3] Jianhong Bai, Menghan Xia, Xiao Fu, Xintao Wang, Lianrui Mu, Jinwen Cao, Zuozhu Liu, Haoji Hu, Xiang Bai, Pengfei Wan, and Di Zhang. Recammaster: Camera-controlled generative rendering from a single video, 2025. 1, 7, 13
- [4] Shuai Bai, Keqin Chen, Xuejing Liu, Jialin Wang, Wenbin Ge, Sibong Song, Kai Dang, Peng Wang, Shijie Wang, Jun Tang, et al. Qwen2. 5-vl technical report. *arXiv preprint arXiv:2502.13923*, 2025. 14
- [5] Yuxuan Bian, Zhaoyang Zhang, Xuan Ju, Mingdeng Cao, Liangbin Xie, Ying Shan, and Qiang Xu. Videopainter: Any-length video inpainting and editing with plug-and-play context control. In *Proceedings of the Special Interest Group on Computer Graphics and Interactive Techniques Conference Conference Papers*, pages 1–12, 2025. 7
- [6] Andreas Blattmann, Tim Dockhorn, Sumith Kulal, Daniel Mendelevitch, Maciej Kilian, Dominik Lorenz, Yam Levi, Zion English, Vikram Voleti, Adam Letts, et al. Stable video diffusion: Scaling latent video diffusion models to large datasets. *arXiv preprint arXiv:2311.15127*, 2023. 1, 2
- [7] Yochai Blau and Tomer Michaeli. The perception-distortion tradeoff. In *Proceedings of the IEEE conference on computer vision and pattern recognition*, pages 6228–6237, 2018. 13
- [8] Tim Brooks, Bill Peebles, Connor Holmes, Will DePue, Yufei Guo, Li Jing, David Schnurr, Joe Taylor, Troy Luhman, Eric Luhman, Clarence Ng, Ricky Wang, and Aditya Ramesh. Video generation models as world simulators. 2024. 1, 12
- [9] Sergi Caelles, Jordi Pont-Tuset, Federico Perazzi, Alberto Montes, Kevis-Kokitsi Maninis, and Luc Van Gool. The 2019 davis challenge on vos: Unsupervised multi-object segmentation. *arXiv:1905.00737*, 2019. 13
- [10] Mathilde Caron, Hugo Touvron, Ishan Misra, Hervé Jégou, Julien Mairal, Piotr Bojanowski, and Armand Joulin. Emerging properties in self-supervised vision transformers. In *Proceedings of the IEEE/CVF international conference on computer vision*, pages 9650–9660, 2021. 5, 13
- [11] Hyungjin Chung, Jeongsol Kim, Michael Thompson Mccann, Marc Louis Klasky, and Jong Chul Ye. Diffusion posterior sampling for general noisy inverse problems. In *International Conference on Learning Representations*, 2023. 2, 12
- [12] Hyungjin Chung, Suhyeon Lee, and Jong Chul Ye. Decomposed diffusion sampler for accelerating large-scale inverse problems. In *The Twelfth International Conference on Learning Representations*, 2024. 2, 5, 13
- [13] Hyungjin Chung, Jong Chul Ye, Peyman Milanfar, and Mauricio Delbracio. Prompt-tuning latent diffusion models for inverse problems. In *International Conference on Machine Learning*, pages 8941–8967. PMLR, 2024. 3
- [14] Hyungjin Chung, Jeongsol Kim, and Jong Chul Ye. Diffusion models for inverse problems. *arXiv preprint arXiv:2508.01975*, 2025. 3
- [15] Zekai Gu, Rui Yan, Jiahao Lu, Peng Li, Zhiyang Dou, Chenyang Si, Zhen Dong, Qifeng Liu, Cheng Lin, Ziwei Liu, Wenping Wang, and Yuan Liu. Diffusion as shader: 3d-aware video diffusion for versatile video generation control, 2025. 1, 2, 13
- [16] Hao He, Yinghao Xu, Yuwei Guo, Gordon Wetzstein, Bo Dai, Hongsheng Li, and Ceyuan Yang. Cameractrl: Enabling camera control for text-to-video generation. *arXiv preprint arXiv:2404.02101*, 2024. 13
- [17] Jonathan Ho, Ajay Jain, and Pieter Abbeel. Denoising diffusion probabilistic models. *Advances in Neural Information Processing Systems*, 33:6840–6851, 2020. 12
- [18] Jonathan Ho, Tim Salimans, Alexey Gritsenko, William Chan, Mohammad Norouzi, and David J Fleet. Video diffusion models. *Advances in Neural Information Processing Systems*, 35:8633–8646, 2022. 1
- [19] Wenbo Hu, Xiangjun Gao, Xiaoyu Li, Sijie Zhao, Xiaodong Cun, Yong Zhang, Long Quan, and Ying Shan. Depthcrafter: Generating consistent long depth sequences for open-world videos, 2024. 3, 5, 6
- [20] Ziqi Huang, Fan Zhang, Xiaojie Xu, Yinan He, Jiashuo Yu, Ziyue Dong, Qianli Ma, Nattapol Chanpaisit, Chenyang Si, Yuming Jiang, et al. Vbench++: Comprehensive and versatile benchmark suite for video generative models. *arXiv preprint arXiv:2411.13503*, 2024. 5
- [21] Hyeonho Jeong, Suhyeon Lee, and Jong Chul Ye. Reangle-a-video: 4d video generation as video-to-video translation, 2025. 2, 4, 5, 6, 13
- [22] Jeongsol Kim, Geon Yeong Park, Hyungjin Chung, and Jong Chul Ye. Regularization by texts for latent diffusion inverse solvers. *arXiv preprint arXiv:2311.15658*, 2023. 4
- [23] Jeongsol Kim, Geon Yeong Park, and Jong Chul Ye. Dream-sampler: Unifying diffusion sampling and score distillation for image manipulation. *arXiv preprint arXiv:2403.11415*, 2024. 4
- [24] Jeongsol Kim, Bryan Sangwoo Kim, and Jong Chul Ye. Flowdps: Flow-driven posterior sampling for inverse problems. *arXiv preprint arXiv:2503.08136*, 2025. 3
- [25] Yuval Kirstain, Adam Polyak, Uriel Singer, Shahbuland Matiana, Joe Penna, and Omer Levy. Pick-a-pic: An open dataset of user preferences for text-to-image generation, 2023. 5, 14
- [26] Weijie Kong, Qi Tian, Zijian Zhang, Rox Min, Zuozhuo Dai, Jin Zhou, Jiangfeng Xiong, Xin Li, Bo Wu, Jianwei Zhang, et al. Hunyuanvideo: A systematic framework for large video generative models. *arXiv preprint arXiv:2412.03603*, 2024. 1
- [27] Taesung Kwon and Jong Chul Ye. Solving video inverse problems using image diffusion models, 2025. 8
- [28] Taesung Kwon and Jong Chul Ye. Vision-xl: High definition video inverse problem solver using latent image diffusion models, 2025. 8
- [29] Black Forest Labs. Flux, 2024. URL <https://blackforestlabs.ai/>. 12
- [30] Black Forest Labs. Flux.1 fill [dev]. <https://huggingface.co/black-forest-labs/FLUX.1-fill-dev>

- Fill-dev, 2025. Model release. License: flux-1-dev-non-commercial-license. 7
- [31] Junnan Li, Dongxu Li, Silvio Savarese, and Steven Hoi. Blip-2: Bootstrapping language-image pre-training with frozen image encoders and large language models. In *International conference on machine learning*, pages 19730–19742. PMLR, 2023. 5, 13
- [32] Teng Li, Guangcong Zheng, Rui Jiang, Tao Wu, Yehao Lu, Yining Lin, Xi Li, et al. Realcam-i2v: Real-world image-to-video generation with interactive complex camera control. *arXiv preprint arXiv:2502.10059*, 2025. 13
- [33] Yaron Lipman, Ricky T. Q. Chen, Heli Ben-Hamu, Maximilian Nickel, and Matthew Le. Flow matching for generative modeling. In *The Eleventh International Conference on Learning Representations*, 2023. 12
- [34] Xingchao Liu, Chengyue Gong, and qiang liu. Flow straight and fast: Learning to generate and transfer data with rectified flow. In *The Eleventh International Conference on Learning Representations*, 2023. 12
- [35] I Loshchilov. Decoupled weight decay regularization. *arXiv preprint arXiv:1711.05101*, 2017. 5
- [36] OpenAI. Openai platform: gpt-5-mini. <https://platform.openai.com/docs/models/gpt-5-mini>, 2025. Accessed on 2025-09-14. 5, 13
- [37] George Papamakarios, Eric Nalisnick, Danilo Jimenez Rezende, Shakir Mohamed, and Balaji Lakshminarayanan. Normalizing flows for probabilistic modeling and inference. *Journal of Machine Learning Research*, 22(57):1–64, 2021. 12
- [38] Jangho Park, Taesung Kwon, and Jong Chul Ye. Zero4d: Training-free 4d video generation from single video using off-the-shelf video diffusion, 2025. 2, 7, 13
- [39] Jordi Pont-Tuset, Federico Perazzi, Sergi Caelles, Pablo Arbeláez, Alex Sorkine-Hornung, and Luc Van Gool. The 2017 davis challenge on video object segmentation. *arXiv preprint arXiv:1704.00675*, 2017. 5
- [40] Alec Radford, Jong Wook Kim, Chris Hallacy, Aditya Ramesh, Gabriel Goh, Sandhini Agarwal, Girish Sastry, Amanda Askell, Pamela Mishkin, Jack Clark, et al. Learning transferable visual models from natural language supervision. In *International conference on machine learning*, pages 8748–8763. PmLR, 2021. 5, 13
- [41] Ron Raphaeli, Sean Man, and Michael Elad. Silo: Solving inverse problems with latent operators. In *Proceedings of the IEEE/CVF International Conference on Computer Vision*, pages 10570–10580, 2025. 3, 4, 5
- [42] Xuanchi Ren, Tianchang Shen, Jiahui Huang, Huan Ling, Yifan Lu, Merlin Nimier-David, Thomas Müller, Alexander Keller, Sanja Fidler, and Jun Gao. Gen3c: 3d-informed world-consistent video generation with precise camera control, 2025. 1, 2
- [43] Robin Rombach, Andreas Blattmann, Dominik Lorenz, Patrick Esser, and Björn Ommer. High-resolution image synthesis with latent diffusion models. In *Proceedings of the IEEE/CVF Conference on Computer Vision and Pattern Recognition*, pages 10684–10695, 2022. 12
- [44] Litu Rout, Negin Raoof, Giannis Daras, Constantine Caramanis, Alex Dimakis, and Sanjay Shakkottai. Solving linear inverse problems provably via posterior sampling with latent diffusion models. *Advances in Neural Information Processing Systems*, 36, 2024. 3
- [45] Saurabh Saxena, Charles Herrmann, Junhwa Hur, Abhishek Kar, Mohammad Norouzi, Deqing Sun, and David J. Fleet. The surprising effectiveness of diffusion models for optical flow and monocular depth estimation, 2023. 6
- [46] Yang Song, Jascha Sohl-Dickstein, Diederik P. Kingma, Abhishek Kumar, Stefano Ermon, and Ben Poole. Score-based generative modeling through stochastic differential equations. In *9th International Conference on Learning Representations, ICLR*, 2021. 12
- [47] Alessio Spagnoletti, Jean Prost, Andrés Almansa, Nicolas Papadakis, and Marcelo Pereyra. Latino-pro: Latent consistency inverse solver with prompt optimization. *arXiv preprint arXiv:2503.12615*, 2025. 3
- [48] Wenqiang Sun, Shuo Chen, Fangfu Liu, Zilong Chen, Yueqi Duan, Jun Zhang, and Yikai Wang. Dimensionx: Create any 3d and 4d scenes from a single image with controllable video diffusion. *arXiv preprint arXiv:2411.04928*, 2024. 13
- [49] Thomas Unterthiner, Sjoerd Van Steenkiste, Karol Kurach, Raphael Marinier, Marcin Michalski, and Sylvain Gelly. Towards accurate generative models of video: A new metric & challenges. *arXiv preprint arXiv:1812.01717*, 2018. 13
- [50] Basile Van Hoorick, Rundi Wu, Ege Ozguroglu, Kyle Sargent, Ruoshi Liu, Pavel Tokmakov, Achal Dave, Changxi Zheng, and Carl Vondrick. Generative camera dolly: Extreme monocular dynamic novel view synthesis. In *European Conference on Computer Vision*, pages 313–331. Springer, 2024. 1, 7, 13
- [51] Team Wan, Ang Wang, Baole Ai, Bin Wen, Chaojie Mao, Chen-Wei Xie, Di Chen, Feiwu Yu, Haiming Zhao, Jianxiao Yang, Jianyuan Zeng, Jiayu Wang, Jingfeng Zhang, Jingren Zhou, Jinkai Wang, Jixuan Chen, Kai Zhu, Kang Zhao, Keyu Yan, Lianghua Huang, Mengyang Feng, Ningyi Zhang, Pandeng Li, Pingyu Wu, Ruihang Chu, Ruili Feng, Shiwei Zhang, Siyang Sun, Tao Fang, Tianxing Wang, Tianyi Gui, Tingyu Weng, Tong Shen, Wei Lin, Wei Wang, Wei Wang, Wenmeng Zhou, Wenten Wang, Wenting Shen, Wenyuan Yu, Xianzhong Shi, Xiaoming Huang, Xin Xu, Yan Kou, Yangyu Lv, Yifei Li, Yijing Liu, Yiming Wang, Yingya Zhang, Yitong Huang, Yong Li, You Wu, Yu Liu, Yulin Pan, Yun Zheng, Yuntao Hong, Yupeng Shi, Yutong Feng, Zeyinzi Jiang, Zhen Han, Zhi-Fan Wu, and Ziyu Liu. Wan: Open and advanced large-scale video generative models, 2025. 1, 4, 6, 12
- [52] Yinhuai Wang, Jiwen Yu, and Jian Zhang. Zero-shot image restoration using denoising diffusion null-space model. In *The Eleventh International Conference on Learning Representations*, 2023. 2
- [53] Zhou Wang, Alan C Bovik, Hamid R Sheikh, and Eero P Simoncelli. Image quality assessment: from error visibility to structural similarity. *IEEE transactions on image processing*, 13(4):600–612, 2004. 4, 13
- [54] Daniel Watson, Saurabh Saxena, Lala Li, Andrea Tagliasacchi, and David J Fleet. Controlling space and time with diffusion models. *arXiv preprint arXiv:2407.07860*, 2024. 13
- [55] Rundi Wu, Ruiqi Gao, Ben Poole, Alex Trevithick, Changxi Zheng, Jonathan T Barron, and Aleksander Holynski. Cat4d:

- Create anything in 4d with multi-view video diffusion models. *arXiv preprint arXiv:2411.18613*, 2024. [1](#), [13](#)
- [56] Zeqi Xiao, Wenqi Ouyang, Yifan Zhou, Shuai Yang, Lei Yang, Jianlou Si, and Xingang Pan. Trajectory attention for fine-grained video motion control. *arXiv preprint arXiv:2411.19324*, 2024. [1](#), [2](#), [4](#), [7](#), [13](#)
 - [57] Dejia Xu, Weili Nie, Chao Liu, Sifei Liu, Jan Kautz, Zhangyang Wang, and Arash Vahdat. Camco: Camera-controllable 3d-consistent image-to-video generation. *arXiv preprint arXiv:2406.02509*, 2024. [13](#)
 - [58] Zhucun Xue, Jiangning Zhang, Teng Hu, Haoyang He, Yinan Chen, Yuxuan Cai, Yabiao Wang, Chengjie Wang, Yong Liu, Xiangtai Li, et al. Ultravideo: High-quality uhd video dataset with comprehensive captions. *arXiv preprint arXiv:2506.13691*, 2025. [5](#)
 - [59] Zhuoyi Yang, Jiayan Teng, Wendi Zheng, Ming Ding, Shiyu Huang, Jiazheng Xu, Yuanming Yang, Wenyi Hong, Xiaohan Zhang, Guanyu Feng, et al. Cogvideox: Text-to-video diffusion models with an expert transformer. *arXiv preprint arXiv:2408.06072*, 2024. [4](#)
 - [60] Meng You, Zhiyu Zhu, Hui Liu, and Junhui Hou. Nvs-solver: Video diffusion model as zero-shot novel view synthesizer. *arXiv preprint arXiv:2405.15364*, 2024. [2](#), [7](#), [13](#)
 - [61] Mark YU, Wenbo Hu, Jinbo Xing, and Ying Shan. Trajectorycrafter: Redirecting camera trajectory for monocular videos via diffusion models, 2025. [1](#), [2](#), [4](#), [7](#)
 - [62] Zhu Zhang, Zhou Zhao, Yang Zhao, Qi Wang, Huasheng Liu, and Lianli Gao. Where does it exist: Spatio-temporal video grounding for multi-form sentences, 2020. [5](#)

Appendix

Supplementary Materials

A. Related Works

A.1. Diffusion and Flow-based Models

Diffusion Models Diffusion models [17, 46] aim to model the data distribution $p(\mathbf{x})$, by learning to reverse forward noising process. The forward process, $q(\mathbf{x}_t|\mathbf{x}_0)$, gradually adds Gaussian noise to a clean data sample \mathbf{x}_0

$$q(\mathbf{x}_t|\mathbf{x}_0) = \mathcal{N}(\mathbf{x}_t; \alpha_t \mathbf{x}_0, \sigma_t^2 \mathbf{I}) \quad (9)$$

where α_t and σ_t (e.g., $\alpha_t^2 + \sigma_t^2 = 1$) are functions of the noise schedule that control the signal-to-noise ratio at time t . To undo one step of this noising, a neural network $\epsilon^\theta(\mathbf{x}_t, t)$ is trained through an epsilon-matching loss:

$$\mathcal{L}_{SM} = \mathbb{E}_{\epsilon \sim \mathcal{N}(0, \mathbf{I}), \mathbf{x}_t \sim p_t} \|\epsilon - \epsilon^\theta(\mathbf{x}_t, t)\|_2^2. \quad (10)$$

Flow-based Models Continuous Normalizing Flows (CNFs) [37] model the continuous transformation between two distributions via an ordinary differential equation (ODE). To circumvent the high computational cost and simulation instability of traditional CNF training, Flow Matching (FM) [33] was introduced:

$$\mathcal{L}_{FM} = \mathbb{E}_{t \in [0,1], \mathbf{x}_t \sim p_t} \|\mathbf{v}_t(\mathbf{x}_t) - \mathbf{v}_t^\theta(\mathbf{x}_t)\|^2. \quad (11)$$

The target velocity field $\mathbf{v}_t(\mathbf{x}_t)$ in Eq. 11 is intractable, as it requires an expectation over the data distribution. Conditional Flow Matching (CFM) [33] solves this by defining a tractable velocity field conditioned on \mathbf{x}_0 :

$$\mathcal{L}_{CFM} = \mathbb{E}_{t \in [0,1], \mathbf{x}_0 \sim q} \|\mathbf{v}_t(\mathbf{x}_t|\mathbf{x}_0) - \mathbf{v}_t^\theta(\mathbf{x}_t)\|^2. \quad (12)$$

With a velocity network \mathbf{v}_t^θ trained on this objective, generation is performed by solving the ODE $d\mathbf{x}_t = \mathbf{v}_t^\theta(\mathbf{x}_t)dt$ from $t = 1$ to $t = 0$. A prominent variant is Rectified Flow [34] which employs a linear interpolation path ($a_t = t$ and $b_t = 1 - t$), resulting in $\mathbf{v}_t(\mathbf{x}_t|\mathbf{x}_0) = \mathbf{x}_1 - \mathbf{x}_0$. Crucially, when the prior distribution p_1 is Gaussian, FM is equivalent to diffusion models². We therefore use these terms interchangeably henceforth.

Latent Diffusion models Training and inference of diffusion models are computationally expensive on high-resolution data. To improve efficiency, these processes can be reformulated in a compressed latent space, as popularized by Latent Diffusion Models (LDMs) [43] and used in most modern diffusion models [8, 29, 51]. A pre-trained Variational Autoencoder (VAE) is used to map data from the pixel space to the latent space ($\mathbf{z} = \mathcal{E}(\mathbf{x})$) and back ($\hat{\mathbf{x}} = \mathcal{D}(\mathbf{z})$). The generative model (ϵ_θ or \mathbf{v}_t^θ) is then trained entirely on the latent representations \mathbf{z} .

A.2. Diffusion Inverse Solvers

Given a pre-trained generative model as a prior $p(\mathbf{x})$, Diffusion Inverse Solvers (DIS) aim to solve inverse problems in Eq. 1. This is achieved by guiding the reverse sampling process to sample from the posterior distribution $p(\mathbf{x}|\mathbf{y})$. A significant advantage of this paradigm is its zero-shot generalization capability; the same pre-trained model $p(\mathbf{x})$ can be applied to various forward operators \mathcal{A} at inference time without re-training. Broadly, these solvers can be categorized by their guidance mechanism.

Backpropagation-Based Solvers One prominent line of work, including Diffusion Posterior Sampling (DPS) [11], guides the sampling at each step t by using the gradient of the data consistency term, $\nabla_{\mathbf{x}_t} \log p(\mathbf{y}|\mathbf{x}_t)$. This is often approximated by $\nabla_{\mathbf{x}_t} \|\mathbf{y} - \mathcal{A}(\hat{\mathbf{x}}_{0|t})\|^2$, where $\hat{\mathbf{x}}_{0|t}$ is the predicted clean data from \mathbf{x}_t . While effective, these methods are computationally prohibitive as they require expensive backpropagation through the deep neural network ϵ^θ (or \mathbf{v}^θ) at every sampling step.

²Set $\alpha_t = 1 - t$, $\sigma_t = t$ in Eq. (9).

Backpropagation-Free Solvers To address the high computational cost, a second line of work seeks to avoid this backpropagation. Decomposed Diffusion Sampling (DDS) [12], for example, synergistically combines diffusion sampling with classical optimization methods. For linear inverse problems, this update is equivalent to solving a proximal optimization problem:

$$\min_{\mathbf{x}} \frac{\gamma}{2} \|\mathbf{y} - \mathcal{A}(\mathbf{x})\|_2^2 + \frac{1}{2} \|\mathbf{x} - \hat{\mathbf{x}}_{0|t}\|_2^2, \quad (13)$$

which can be solved efficiently using a small number of Conjugate Gradient (CG) steps. This approach eliminates the need to compute the costly Manifold-Constrained Gradient (MCG), resulting in dramatic accelerations.

A.3. Novel View Synthesis

Early efforts to imbue VDMs with precise camera control involved modifying the model architecture or training process. This included training external modules to inject conditioning information such as camera parameters [16, 32], conditioning the model on explicit geometric representations like Plücker embeddings [1, 55], or inflating the attention mechanisms of the base VDM [2, 48, 54, 57].

Video-to-Video Translation for Camera Control More recently, the problem has been effectively framed as a video-to-video translation task. The first and most common direction involves fine-tuning a pre-trained VDM. This includes methods that train the model to directly accept camera parameters as input conditions [3, 50, 55], or methods that tries to solve a 3D-aware inpainting problem [15, 21, 56]. These methods warp the source video according to the target trajectory and then fine-tune the VDM to realistically inpaint the resulting occluded or disoccluded regions. The second, training-free methods adapt pre-trained VDMs as powerful generative priors, typically by reformulating the task as an inverse problem that can be solved at inference time [38, 60]. Our work builds upon this paradigm by developing a more efficient and robust latent-space solver for this task.

B. Implementation Details

B.1. Text-guided Inpainting Dataset

The Text-guided Inpainting dataset consists of video clips, target masks, source prompts, and target prompts. We selected 20 videos and target mask pairs from the DAVIS [9] dataset. In each pair, the foreground in the mask is treated as the inpainting target. For source prompt generation, we used the BLIP-2 [31] model to generate a caption describing the middle frame of each video. The target prompts were then generated using the gpt-5-mini-2025-08-07 [36] model, which took the source prompt as input along with the following instruction prompt (Fig. 9). A total of five target prompts were generated for each video, resulting in a dataset containing 125 samples.

B.2. Evaluation Metric

For the quantitative comparison, we evaluate following metrics following the evaluation code^{3 4 5 6}:

1. Measurement PSNR : We compute the PSNR by excluding the masked region, resulting in the measurement PSNR.
2. Measurement LPIPS : We measure the LPIPS [7], which is defined as distance between feature maps of pre-trained VGG network, by excluding the masked region.
3. Measurement SSIM : We compute the structural similarity [53] by excluding the masked region.
4. DINO distance : We evaluate source distribution consistency by computing the average cosine distance between DINO-ViT [10] features extracted from the generated video and the source video.
5. FVD : We report the Fréchet Video Distance (FVD) [49] to assess the overall quality and temporal coherence of the generated videos, using features from a pre-trained I3D network.
6. VBench: We calculate subject consistency, temporal flickering, motion smoothness for Quality Score and overall consistency for Semantic Score, calculate the Total Score based on the metric weights & normalization method in VBench.
7. CLIP-score : We report the similarity between features embedded by pre-trained CLIP [40]⁷ image encoder and text encoder.

³<https://github.com/cure-lab/PnPInversion/tree/main/evaluation>

⁴<https://github.com/yuvalkirstain/PickScore>

⁵https://github.com/JunyaoHu/common_metrics_on_video_quality

⁶<https://github.com/Vchitect/VBench>

⁷We use CLIP ViT-base-patch16.

Prompt for Inpainting Target Prompt Generation

You are an AI assistant for generating paired text prompts for real image editing tasks. Your goal is to modify a given text description by replacing an object with other while strictly following these rules:

- 1) Modify the primary object that appears in the original prompt. There is only one primary object in the image.
- 2) The replacement must be significantly different from the original concept but contextually appropriate. Avoid unrealistic substitutions (e.g., changing ‘rabbit on grass’ to ‘rocket on grass’).
- 3) Ensure diversity in word choices across different modifications.
- 4) Preserve all other words exactly as they are. Do not change sentence structure, introduce new elements, or modify additional details.
- 5) Do not provide any additional words—output only the modified text description.
- 6) Editing is done by masking the primary object and filling in only that area (text-guided inpainting). In other words, it is not possible if the silhouette of the target object differs too much, so please avoid creating target prompts that result in such discrepancies.

The output format must be like this: ["<modified prompt1>", "<modified prompt2>", "<modified prompt3>", "<modified prompt4>", "<modified prompt5>"]. You must generate **5** different versions of the modified prompt.

original prompt: {text}

Figure 9. Prompt used for text-guided inpainting prompt generation with GPT-5-mini. Given a source prompt describing the initial video frame, the model is instructed to generate diverse and contextually consistent target prompts to construct the inpainting dataset.

8. Pick-score : To measure the alignment between the generated video and the target text prompt, we use the Pick-score [25] to predict human preferences, providing a proxy for both text-video alignment and aesthetic quality.
9. VLM : We discuss about this in the following section.

B.2.1. VLM metric

To assess both the visual quality of the generated videos and their alignment with the target text prompt, we employ a Vision Language Model (VLM)-based evaluation metric. Specifically, we use Qwen2.5-VL-3B-Instruct [4], which is capable of processing video input natively. The VLM is prompted to evaluate each video-prompt pair across three criteria in equal weight: (1) faithfulness to the prompt, (2) visual quality, and (3) temporal coherence. The model outputs a score between 0 and 10, which we normalize to the range of 0 to 1 for reporting. The full evaluation prompt provided to the VLM is shown in Fig. 10.

Prompt for VLM Evaluation Metric

You are an expert video evaluator. Your task is to judge a video based on three equally weighted aspects:

1. **Faithfulness to Prompt**: Does the video accurately reflect the user’s input prompt in terms of objects, attributes, style, and composition?
2. **Visual Quality**: Is the video clear, sharp, and free from any unrealistic artifacts or distortions?
3. **Temporal Coherence**: Is the video smooth and coherent over time, without abrupt changes or jarring transitions?

Please rate this video on a scale of 0-10 (10 being perfect) and explain your reasoning. Please put your score in <score> score </score>. Prompt: {pr}

Figure 10. Evaluation prompt used for VLM-based scoring with Qwen2.5-VL-3B-Instruct. The model is given a generated video and its corresponding text prompt, and returns a score reflecting prompt faithfulness, visual quality, and temporal coherence.

B.3. Conjugate Gradient Algorithm

We provide the pseudo-code of the Conjugate Gradient method in Algorithm 2. We used $\text{CG}(\mathbf{A}, \mathbf{y}, \mathbf{x}, K)$ in the paper to imply running K steps of conjugate gradient steps with initialization \mathbf{x} .

Algorithm 2 Conjugate Gradient (CG)

Require: $\mathbf{A}, \mathbf{y}, \mathbf{x}_0, M$

```
1:  $\mathbf{r}_0 \leftarrow \mathbf{b} - \mathbf{A}\mathbf{x}_0$ 
2:  $\mathbf{p}_0 \leftarrow \mathbf{b}_0$ 
3: for  $i = 0 : K - 1$  do
4:    $\alpha_k \leftarrow \frac{\mathbf{r}_k^\top \mathbf{r}}{\mathbf{p}_k^\top \mathbf{A} \mathbf{p}_k}$ 
5:    $\mathbf{x}_{k+1} \leftarrow \mathbf{x}_k + \alpha_k \mathbf{p}_k$ 
6:    $\mathbf{r}_{k+1} \leftarrow \mathbf{r}_k - \alpha_k \mathbf{A} \mathbf{p}_k$ 
7:    $\beta_k \leftarrow \frac{\mathbf{r}_{k+1}^\top \mathbf{r}}{\mathbf{r}_k^\top \mathbf{r}_k}$ 
8:    $\mathbf{p}_{k+1} \leftarrow \mathbf{b}_{k+1} + \beta_k \mathbf{p}_k$ 
9: end for
10: return  $\mathbf{x}_K$ 
```

C. Additional Results

C.1. Visualization of latent mask

Fig. 11 compares the latent masks produced by conventional binary downsampling against those from InverseCrafter. The naive resizing approach yields a single-channel, binary mask that is uniformly broadcast across all C channels. In contrast, our method generates a continuous, C -channel mask, preserving distinct spatio-temporal information for each latent feature.

C.2. Additional Qualitative Comparison

We provide further qualitative results, demonstrating our method’s performance against baseline methods. Fig. 12 and 13 present results for the video camera control task, fig. 14 and 15 shows results for the video inpainting with editing task.

C.3. Runtime Comparison

In this section, we validate the computational efficiency of InverseCrafter by comparing its wall-clock inference time against the baseline Video Diffusion Model (VDM). Consistent with the claims made in the main text, our results demonstrate that the proposed method incurs negligible runtime overhead. Our evaluation focuses specifically on the execution time of the diffusion transformer during the latent-space ODE solving process. Experiments were conducted on a workstation equipped with an AMD EPYC 7543 32-Core Processor and an NVIDIA RTX A6000 GPU.

| Method | Ours ($\alpha = 0.6$) | Base ($\alpha = 0.0$) |
|---------------|-------------------------|-------------------------|
| Runtime (sec) | 71 | 70 |

Table 3. Runtime Comparison.

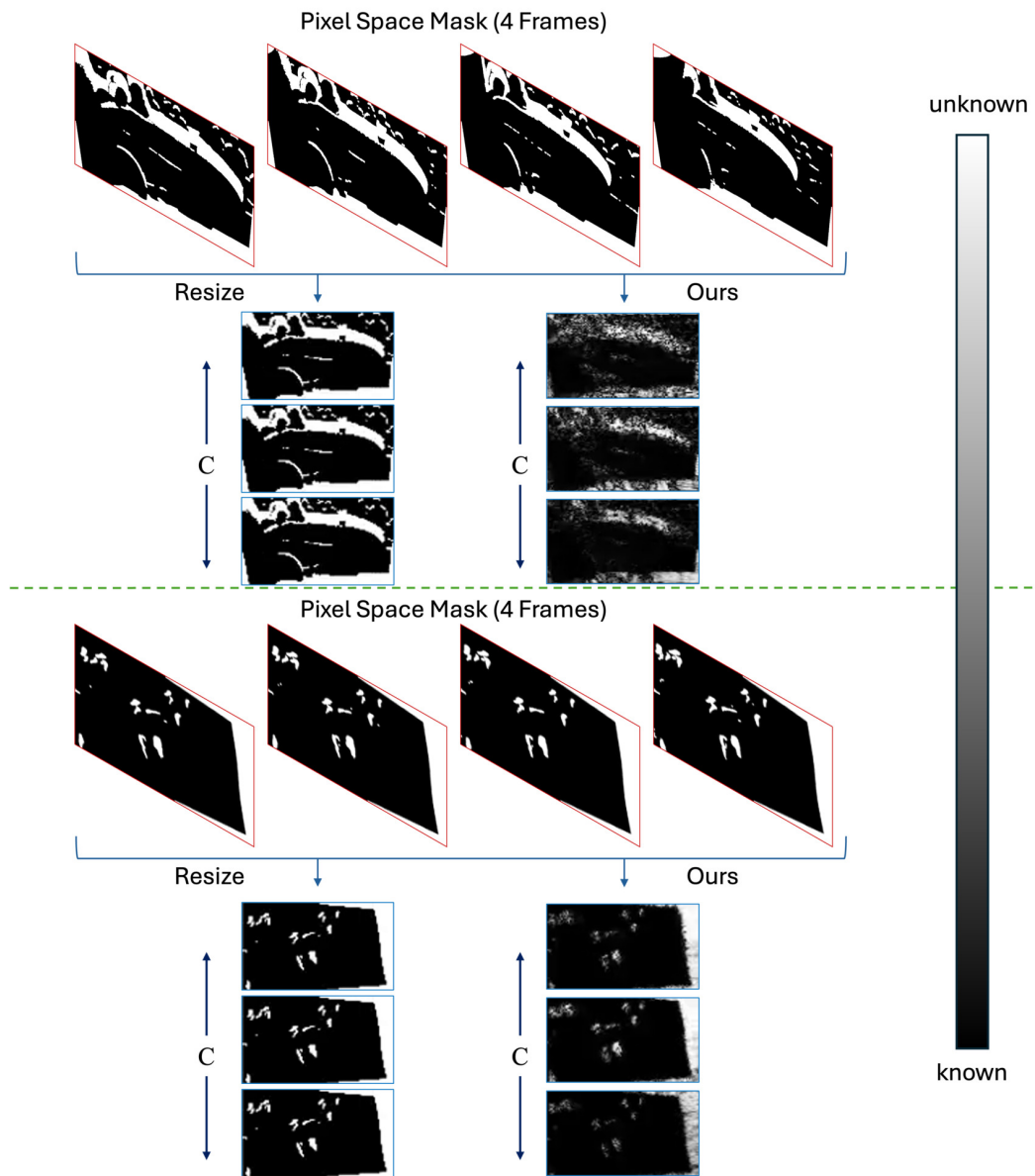


Figure 11. Comparison of latent mask generation process.



Figure 12. Additional qualitative comparison of video camera control.

Figure 13. **Additional qualitative comparison of video camera control.**



*“a **brown bear** walking on rocks” → “a **young stag** walking on rocks”*

Figure 14. **Additional qualitative comparison of video inpainting with editing.** NVS-Solver indicates NVS-Solver (post), NVS-Solver* indicates NVS-Solver (dgs).



“a rhino is standing in the dirt near rocks→ “an elephant is ...”

Figure 15. **Additional qualitative comparison of video inpainting with editing.** NVS-Solver indicates NVS-Solver (post), NVS-Solver* indicates NVS-Solver (dgs).